Solid state dewetting of Ag/Pt bilayers for the stronger localized surface plasmon resonance (LSPR) properties: The dynamic control of surface morphology and elemental composition of AgPt and Pt nanostructures by the auxiliary Ag layer

Puran Pandey, Sundar Kunwar, Jihoon Lee[*]

Department of Electronic Engineering, College of Electronics and Information, Kwangwoon University, Nowon-gu Seoul, 01897, South Korea

ABSTRACT

The modification and control of localized surface plasmon resonance (LSPR) properties of metallic nanoparticles (NPs) has become a vigorous research focus in various fields due to its wide range of applicability in various applications, which can be achieved by the control of surface morphology and elemental composition. In this paper, various configurations and compositions of AgPt and Pt NPs are demonstrated by the solid state dewetting using an auxiliary Ag layer on sapphire (0001) along with their strong dynamic LSPR properties. By the systematic control of Ag/Pt bilayer thickness and temperature, the interconnected AgPt nanoclusters at low temperature (<600 °C) and well-isolated pure Pt NPs at higher temperature (>650 °C) are obtained based on the enhanced diffusion, alloying, surface energy minimization and Ag sublimation. A strong LSPR response in the UV and VIS region is exhibited by the AgPt and Pt NPs depending on the alteration of size, shape, uniformity and elemental compositions. In particular, the AgPt NPs show the stronger plasmonic responses and it gradually attenuates with the sublimation of Ag atoms which results in the development of Pt NPs. In comparison with the previous study on the pure Pt NPs on sapphire, the Pt NPs in this study are significantly improved in terms of shape, size and spacing, whose LSPR responses are much stronger and dynamic. The auxiliary diffusion enhancement by Ag atoms leads to the rapid dewetting of AgPt NPs while the Ag sublimation assists the evolution of well-developed Pt NPs due to the vacancy creation and removal of material during mass transport. The tunability of surface morphologies and LSPR properties of AgPt and Pt NPs are systematically demonstrated by the methodical control of Ag/Pt bilayer thickness.

© 2019 Elsevier B.V. All rights reserved.

1. Introduction

Metallic nanoparticles (NPs) are the subject of immense research interests in the fields of energy, sensor, biomedicine, catalysis and energy storage applications due to their largely tunable optical, electronic, magnetic, sensing and catalytical properties [1—7]. By the appropriate control and design of NPs, one can modify/optimize the related properties and thus the applicability in the device applications. Meanwhile, the integration of multiple metallic elements in a single NP can provide additional opportunity to diversify the applications and tune-abilities of NPs based on the variation of elemental compositions. In recent years, the metallic NPs have offered various useful applications due to their strong interactions with photons, known as the localized surface plasmon resonance (LSPR) [8—10]. The LSPR is a collective electron oscillation in the NPs at the resonant frequency, which can be readily tuned by the control of NP configuration and elemental composition [11]. The LSPR effect of metallic NPs have been exploited to enhance the light absorption, catalytic activity and sensitivity in the photovoltaic cells, photocatalysis and biosensors respectively [9—12]. For instance, the power conversion efficiency and short current density of polymer solar cell has been significantly enhanced by the strong LSPR effect in the Cu NPs that exhibited a broad absorption in the UV to NIR wavelength [13]. Despite the numerous advantages of monometallic NPs, the integration of multiple metallic components in a single NPs have drawn a further research attention in various fields because of their

superior properties such as multifunctionality, structural tunability and elemental heterogeneity. As an example, the plasmon resonance bandwidth of Ag NPs have been readily extended from the UV to the NIR wavelength by alloying with Au, which resulted in a significant efficiency improvement in polymer solar cells [14–16].

Among various noble metallic NPs, the Pt NPs generally exhibit weaker LSPR response, however, they have been considered as a promising material in catalysis due to its robustness and high catalytic responses [17,18]. Thus, the integration of Pt NPs with a strong plasmonic material such as Ag can be a useful approach to improve the performance of related applications. At the same time, the solid state dewetting (SSD) of pure Pt films on a substrate often yields irregular and large surface coverage of Pt nanoclusters due to the low diffusivity and high surface energy of Pt atoms [19,20]. To enhance the structural and plasmonic properties of Pt NPs, the SSD of Pt films along with the auxiliary Ag component can be a very handy approach, which however has not been realized to date.

In this paper, the SSD of Ag/Pt bilayer films has been systematically performed to yield various AgPt and Pt NPs on a transparent c-plane sapphire and their LSPR properties are accordingly revealed by the optical characterizations along with the finite difference time domain (FDTD) simulations. The growth mechanism of AgPt and Pt NPs is proposed as the combinational result of the temperature driven atomic diffusion, alloying, surface energy minimization and Ag atom sublimations as illustrated in Fig. 1. By the systematic control of the annealing temperature, bilayer thickness, Ag and Pt ratio, various configuration and size of AgPt and Pt NPs are demonstrated. Consequently, the improved surface morphology, as well as strong LSPR properties of AgPt and Pt NPs, has been realized in terms of the size, shape and uniformity as well as the dynamic LSPR responses in the UV-VIS regions.

2. Experimental section

In this work, both-side polished 430 μm thick c-plane sapphire (0001) (iNexus, South Korea) with ±0.1° off-axis were utilized as a substrate. Firstly, the sapphire substrates were degassed in order to remove the trapped water vapors, particles and oxides on the surface. The degassing was performed in a pulsed laser deposition chamber (PLD) (DaDa TG, South Korea)) at 600 °C for 30 min under 1×10^{-4} Torr. The degassed sapphire was examined with an atomic force microscope (AFM) (Park Systems, South Korea) as shown in Fig. S1, which show the surface height within ±2 nm and roughness of 0.1 nm.

Then, the cleaned substrate was used for the deposition of metallic films by sputtering. In this experiment, the Ag/Pt bilayer design was adapted: i.e. the Ag film was deposited first and then Pt film was added atop. In total, three different Ag/Pt bilayers configurations were fabricated: i.e. $Ag_{14 nm}/Pt_{3 nm}$, $Ag_{42 nm}/Pt_{9 nm}$ and $Ag_{50 nm}/Pt_{25 nm}$. Both the Ag and Pt films were deposited with the growth rate of 0.05 nm/s at the ionization current 3 mA: i.e. 20 s = 1 nm. The purity of metal targets used for deposition was 99.999%. To grow the surface nanostructures, the Ag/Pt bilayer deposited samples were transferred to the PLD chamber and
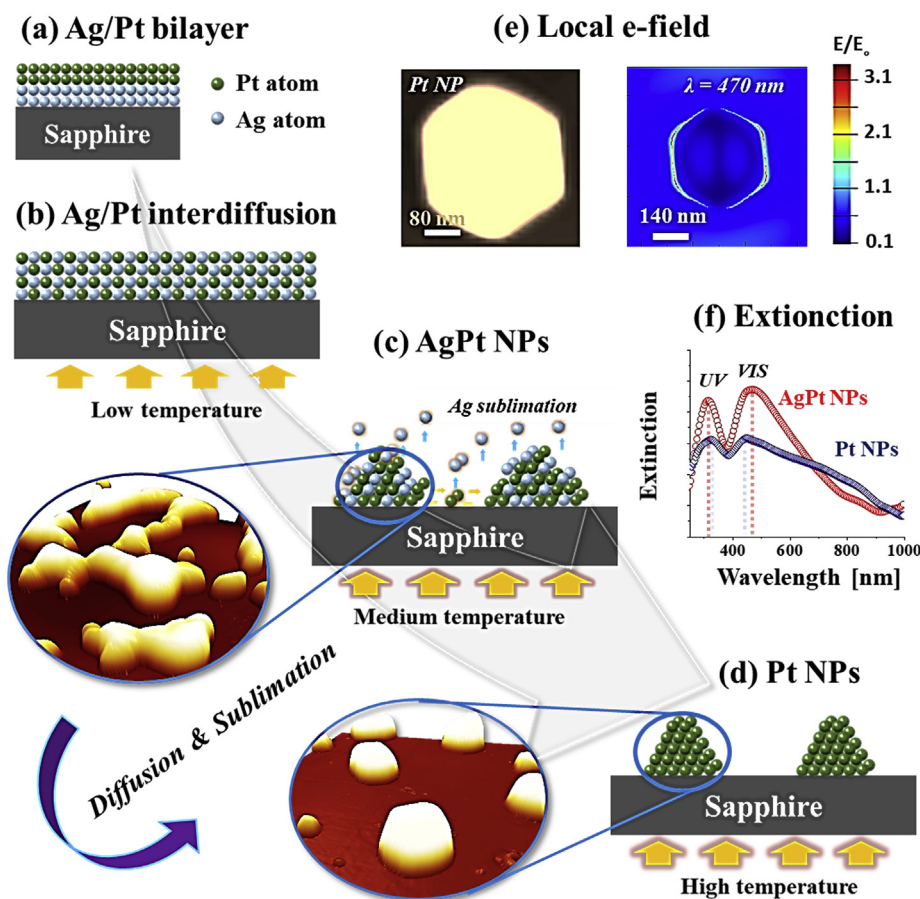

Fig. 1. Fabrication of AgPt and Pt nanoparticles (NPs) on sapphire (0001) by the systematic annealing of Ag/Pt bilayers. (a) Schematic of Ag/Pt bilayer deposition. (b) Atomic interdiffusion induced at relatively lower temperature annealing. (c) Formation of AgPt alloy NPs at medium temperature. (d) Evolution of well developed Pt NPs after Ag sublimation at high temperature. (e) Local e-field distribution of typical Pt NP. (f) Comparison of extinction of typical AgPt and Pt NPs.

systematically annealed at the pre-determined temperatures between 500 and 900 °C. The annealing chamber pressure was about 1×10^{-4} Torr before turning on the heating system. The system temperature was ramped at 4 °C/s to reach the predefined target temperatures (Ta). After reaching the Ta, the constant dwelling time of 120 s was allocated for the matured growth of NPs. To finish the growth process, the heating system was fully turned off and samples were kept under vacuum until the system temperature reached to ambient.

The surface morphology of various AgPt and Pt NPs was captured by an AFM and scanning electron microscope (SEM) (CX-200, COXEM, South Korea). The AFM was operated under non-contact mode at an ambient environment and the same batch of AFM tips were used for scanning in order to minimize tip effects. The elemental analysis of the AgPt and Pt NPs was performed by the energy-dispersive x-ray spectroscope (EDS) (Noran System 7, Thermo Fisher, United States of America). The optical properties were characterized by the NOST system (Nostoptiks, South Korea), integrated with ANDOR sr500i spectrograph and deuterium-halogen lamp. The reflectance and transmittance spectra were experimentally measured, and the extinction was extracted by: E % = 100% - (R + T) %. In addition, the e-field distribution and extinction spectra of various AgPt and Pt NPs on sapphire were simulated by using the finite difference time domain (FDTD) solver (Lumerical, Canada). For the complex refractive index of pure Ag and Pt, Palik's and Rakic experimental data were followed [21,22]. For AgPt alloy particles, the material constant was averaged form the pure Ag and Pt based on the atomic % of elements [23,24]. In specific, the 3D AFM images of typical NP was imported as a simulation object, which is surrounded by the perfectly matched layer boundary conditions in x, y, z-directions. The total field scattered field (TFSF) source between 250 and 1100 nm was used for the optical excitation. The simulation was performed in air with the mesh size of 0.1−2 nm and auto shutoff level of 10^{-6}.

3. Result and discussion

Fig. 1 shows the overall growth process of AgPt and Pt NPs on sapphire (0001) by the systematic annealing of Ag/Pt bilayers under the vacuum environment. The stepwise evolution of well-defined and isolated NPs from the continuous Ag/Pt bilayer is illustrated by schematics in Fig. 1(a) − 1(d). Since the annealing of Ag/Pt bilayer was performed well below the melting point of both Ag and Pt, the morphological transformation was expected to occur based on the solid-state dewetting (SSD) [25]. In the case of monometallic thin film on a substrate, it generally can be in the unstable or metastable stage after the deposition and tend to agglomerate into the particles upon annealing [26]. The SSD of thin films can be induced by the atomic diffusion and driven by the surface and interface energy minimization. In the case of metallic bilayers, the atomic interdiffusion, diffusivity variation, lattice mismatch, surface energies and interface energies may also affect the dewetting process [27−30]. From the previous report on the dewetting of Ag and Pt on sapphire, the Ag films showed well-developed NPs even at ~300 °C while mostly irregular-connected Pt nanoclusters were resulted up to 900 °C with the similar film thickness and growth conditions [31]. This is due to the fact that the diffusivity of Ag atoms is significantly higher than Pt atoms. Furthermore, the surface and interface energy of Ag atoms with the sapphire are relatively lower compared to the Pt atoms [32]. The Ag and Pt atoms are immiscible in the bulk phase due to the wide miscibility gap and huge variation in melting points but they can well intermix to form an alloy in nanoscale [33].

The schematic in Fig. 1(a) show the deposition of Ag/Pt bilayer, in which the Ag was deposited first in order to facilitate the

dewetting process since the Ag atoms has a higher diffusivity than the Pt and possess a less interfacial energy with the sapphire as discussed. At a low annealing temperature (Ta), the Ag and Pt atoms can inter-diffuse through the interface as shown in Fig. 1(b), resulting in an increased concentration of Ag atoms in the Pt layer and vice-versa. Eventually, due to the enhanced global diffusion of atoms, the interface can be completely consumed and homogeneously intermixed or alloyed AgPt layer can be formed at an increased Ta. Depending upon the Ta and thickness of the bilayers, the extent of interdiffusion of atoms in the adjacent metal layers and alloy formation can be affected. As a sufficient thermal energy is provided, the void formation and agglomeration of the AgPt alloy atoms can give a rise to the formation of AgPt NPs as presented in Fig. 1(c). Meanwhile, due to the high vapor pressure of Ag, the sublimation of Ag atoms can also occur simultaneously. This may result in the more dynamic evolution and unique surface configurations of NPs as compared to the pure metal film dewetting [34]. The Ag sublimation can accelerate the dewetting process much faster due to the vacancy creation and removal of atoms during the mass transport. Thus, the Ag atoms essentially accelerates the overall dewetting process and preferentially sublimate to form the well-developed and isolated Pt NPs as shown in Fig. 1(d). Meanwhile, due to the structural and elemental transformation of NPs, the corresponding optical responses was also significantly altered as the plasmonic mode varies with the configurations and composition of NPs as shown in Fig. 1(e) and (f). The various surface morphologies and corresponding optical behaviors of AgPt and Pt NPs have been thoroughly investigated in the following sections.

Fig. 2 show the detailed analysis on the dewetting characteristics of $Ag_{14\,nm}/Pt_{3\,nm}$ films by the AFM images, cross-sectional line profiles, RMS roughness (Rq) and surface area ratio (SAR) plots. Corresponding elemental analysis of each sample is presented by the at % of elements (Ag and Pt) and EDS spectra at specific temperatures. In addition, the large-scale AFM images and EDS spectra are provided in the Supplementary Figs. S2−S3. Initially, at 500 °C, the irregular-connected AgPt NPs of 100 nm height and 500 nm width were obtained as shown in Fig. 2(a). Along with the increased annealing temperature (Ta), the surface morphology of AgPt alloy NPs was gradually transformed by the void coalescence and compact agglomeration of atoms, which resulted in the isolated AgPt NPs at 550 °C as shown in Fig. 2(b). The average height and width of NPs were estimated to be ~70 and 300 nm respectively as shown by the cross-sectional line profile. Similarly, the Rq was slightly decreased from 19.23 to 18.7 nm as displayed in Fig. 2(g) due to the height reduction of NPs. However, the SAR was slightly increased from 11.23 to 14.25% as shown in Fig. 2(h), which can be due to the formation of a greater number of isolated NPs. The evolution of isolated NPs from the connected nanoclusters can be described by the Rayleigh-like instability and interface energy minimization [27−30]. Generally, with the enhanced agglomeration of atoms at higher temperature, the larger size can be expected. On the contrary, however, smaller NPs were obtained in this work, which was due to the corresponding sublimation of Ag atoms and as well as continues fragmentation of NP clusters.

Fig. 2(i) shows the summary of elemental composition of Ag and Pt in terms of atomic (at) % and the corresponding EDS spectra are provided in Fig. S3. It was observed that the at % of Ag was reduced from ~90 to 84% between 500 and 550 °C. At the Ta of 600 °C and above, the at % of Ag was zero while the at % of Pt was 100%. This can be due the exponential increase in the rate of Ag sublimation with Ta, which caused a complete desorption of Ag atoms above 600 °C. In addition, the EDS spectra of samples annealed at 500 and 900 °C clearly showed the sublimation of Ag atoms. Along with the sublimation of Ag atoms, the surface morphology of NPs was largely transformed such as the isolated NPs with the sharp reduction in
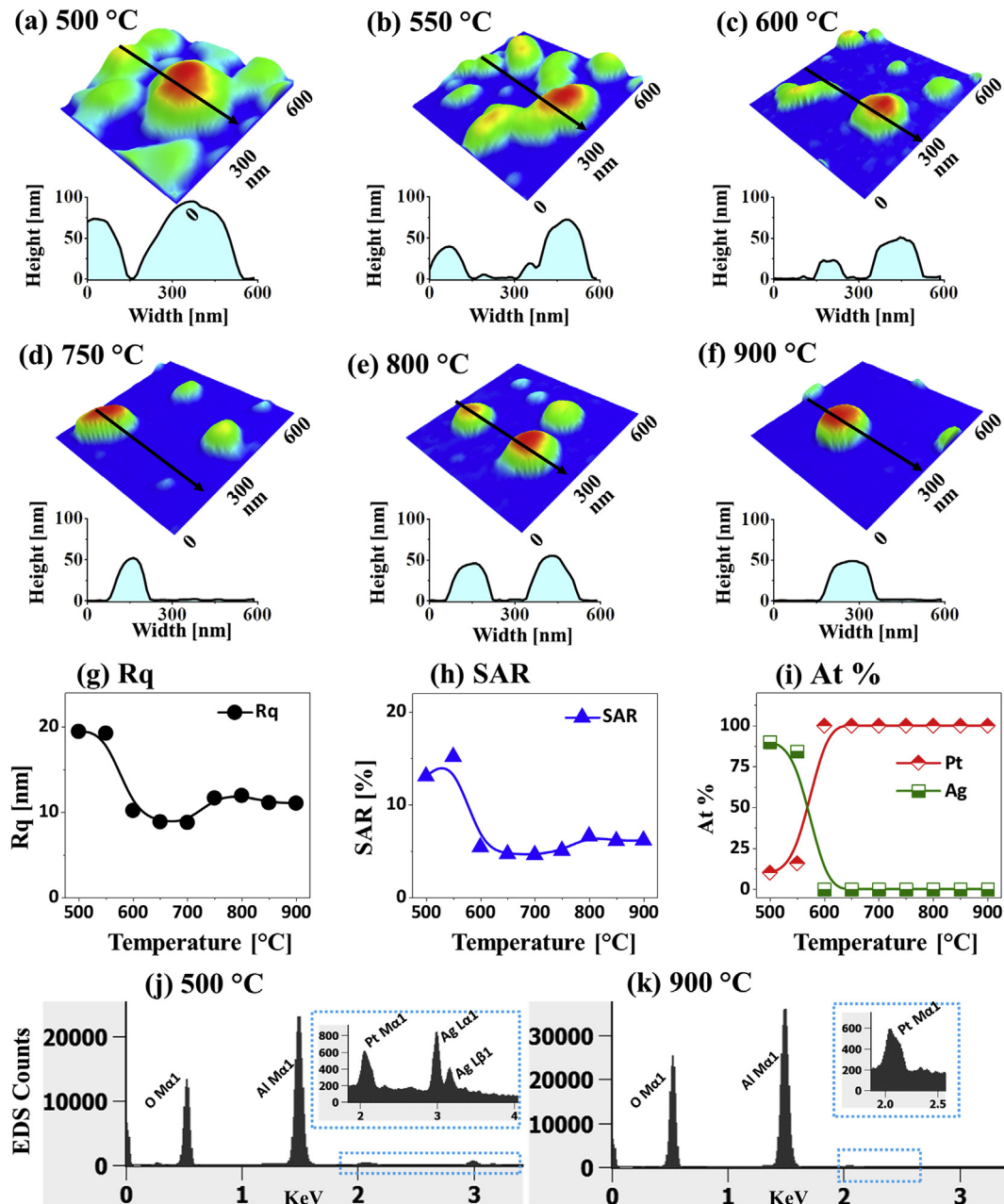
Fig. 2. Evolution of AgPt and Pt NPs on sapphire (0001) with the Ag$_{14\,nm}$/Pt$_{3\,nm}$ bilayers by annealing between 500 and 900 °C for 120 s. (a)–(d) Schematic illustration of AgPt and Pt NP evolution. (e)–(j) AFM images (3 × 3 μm^2) along with the line profiles of AgPt and Pt NPs. (k)–(l) Summary plots of RMS roughness (Rq) and surface area ratio (SAR). (j) Plot of atomic (at) % of Ag and Pt. (n)–(o) Energy dispersive x-ray spectroscope (EDS) spectra of 500 and 900 °C samples.

size as shown in Fig. 2(c) - 2(f).

The average size of Pt NPs was found to be 200 nm in width and 50 nm in height. Similarly, the Rq and SAR were sharply decreased due to the size decrement between 600 and 750 °C. At the higher Ta, the change of Pt NPs occurred mildly as the average size of NPs was slightly increased and became more regular. This process can be driven by the surface energy minimization of NPs and natural tendency to attain the thermodynamically equilibrium configurations at favorable diffusion. Overall, the Ag atoms in the Ag/Pt bilayer films largely enhanced the dewetting process and preferentially sublimated from the NP matrix. The Pt NPs in this work are significantly improved as compared to the pure Pt film dewetting in terms of the shape, size and spacing [15,31]. In specific, these Pt NPs possessed larger size, regular configuration and wide spacing as compared to those obtained with the pure Pt film in the previous studies.

Fig. 3 shows the optical properties of various AgPt alloy and Pt NPs fabricated with the Ag$_{14\,nm}$/Pt$_{3\,nm}$ bilayers in terms of extinction, reflectance and transmittance spectra. In addition, the local e-field profiles and extinction spectra of typical AgPt and Pt NPs were simulated using the FDTD solutions. In general, the large AgPt nanoclusters and semi-spherical smaller Pt NPs demonstrated the distinct optical behaviors. For instance, the extinction spectra demonstrated a minor peak at UV (~315 nm) and another broad peak at VIS region (~500 nm) with the large AgPt nanoclusters as shown by Fig. 3(a). In addition, the normalized extinction of the AgPt and Pt NPs are presented in Figs. 3(a-1) and 3(a-2) respectively. Since the AgPt nanocluster possessed a wide coverage with
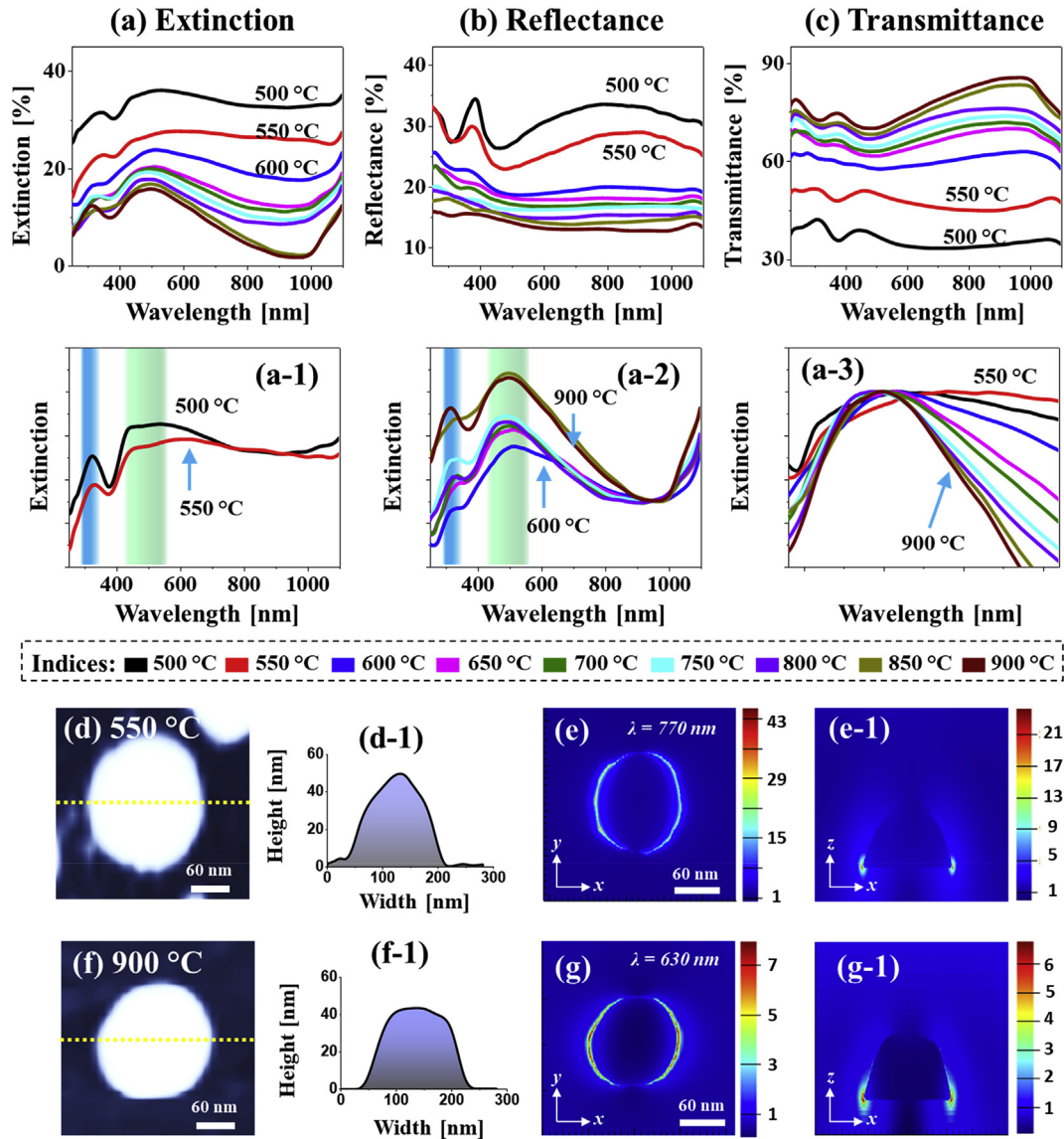
Fig. 3. LSPR properties of various AgPt and Pt NPs with the Ag$_{14 \text{ nm}}$/Pt$_{3 \text{ nm}}$ bilayers. (a)–(c) Extinction, reflectance and transmittance spectra. (a-1) − (a-3) Normalized extinction spectra. (d) and (f) AFM images of typical AgPt and Pt NPs selected for the finite difference time domain (FDTD) simulation. (d-1) and (f-1) Cross-sectional line profiles. (e) and (g) E-field profiles in xy-plane. (e−1) and (g-1) E-field profiles in xz-plane.

the large size over 300 nm, the excitation of UV and VIS peaks can be assigned to the higher order (HO) and multipolar (MP) resonance respectively [35]. As the annealing temperature (Ta) was increased between 500 and 550 °C, the LSPR peaks were slightly decreased likely due to the Ag sublimation as well as the size reduction of alloy nanoclusters. The corresponding E-filed profile of AgPt NP (~150 nm diameter and 50 nm height) at 550 °C was simulated as shown in Fig. 3(d) − 3(e), which generally showed the strong e-field confinement at the boundary of NPs. Furthermore, the extinction power spectra are simulated in Fig. S4, which exhibited a strong dipolar peak at 770 nm. The simulated extinction maxima was largely red-shifted as compared to the measured spectra, which could be due to the larger size of the AFM imported NP. Furthermore, the real sample has wider size distribution of AgPt NPs and thus the plasmon resonance wavelength can vary with size and finally overlapped peak will be observed in the measured spectra. It was also observed that the dipolar resonance was the most prominent in the visible region with the typical AgPt NP,

which is clearly shown by the e-field vector plot with the vector directions along the axis. When the smaller size (<150 nm in diameter) Pt NPs were formed above 600 °C after the complete Ag sublimation, the LSPR peaks in UV and VIS regions were sharply altered as shown in Figs. 3(a-2). In fact, the LSPR peaks were significantly narrower and blue shifted. As the size of Pt NPs was sharply reduced from the AgPt nanoclusters, the UV and VIS peaks can be mainly contributed by the quadrupolar (QR) and dipolar (DR) resonance modes [36]. As the overlapping effect of various resonance modes can be diminished with the smaller size and improved uniformity, the resonance peaks may appear sharper at the resonance wavelengths.

For the Pt NPs fabricated between 600 and 900 °C, the trend of blue shift and narrowing effect was traced with the DR peak as presented in Fig. 3(a-3). Fig. 3(f) − 3(g) depict the corresponding e-field distribution of typical Pt NPs, which clearly show the strong e-field intensity due to the strong dipolar resonance mode. The simulated e-field of Pt NP also exhibited a sharp reduction in the
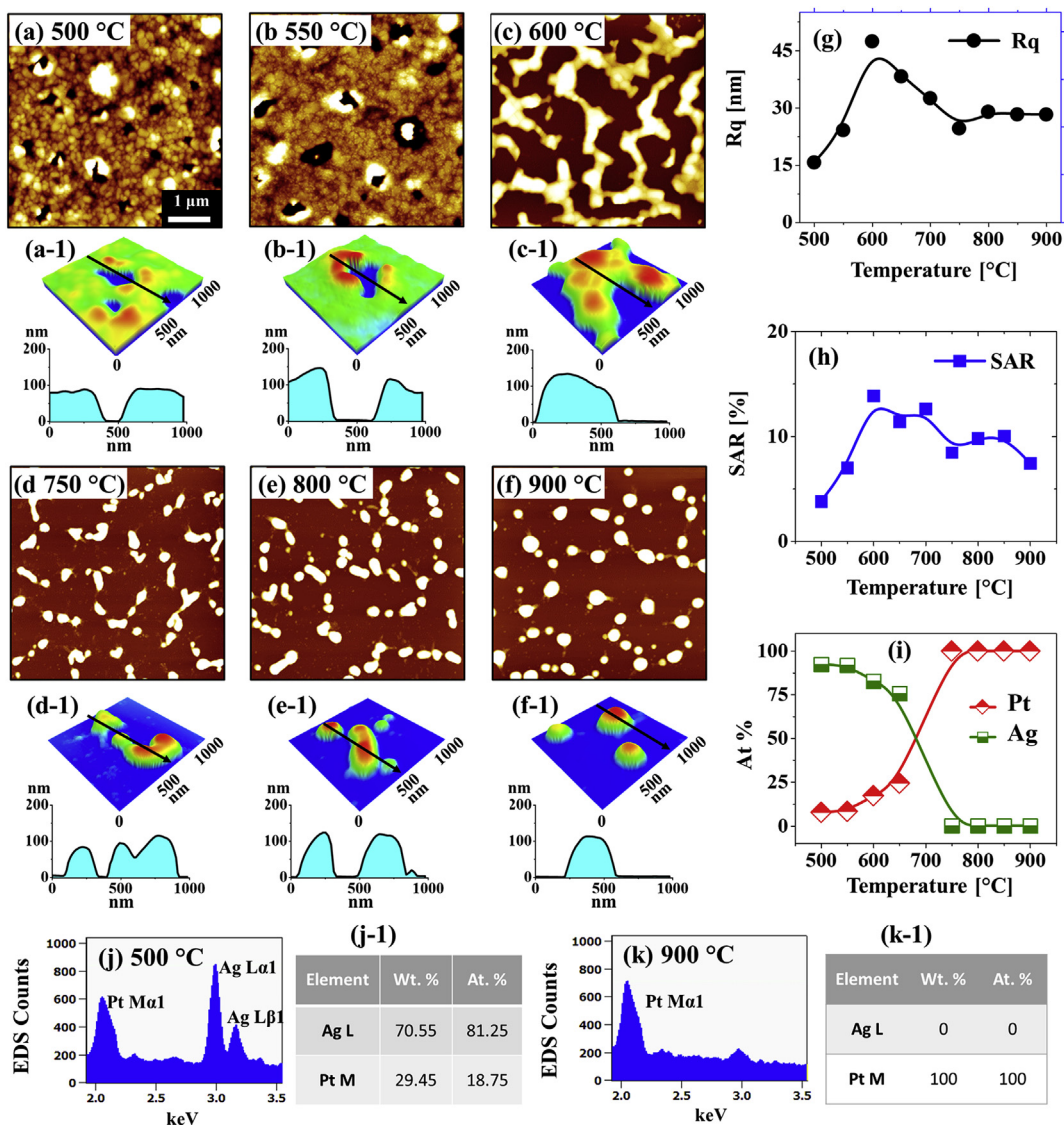
Fig. 4. Evolution of AgPt alloy nanoclusters to isolated Pt NPs on sapphire (0001) with the $Ag_{42\ nm}/Pt_{9\ nm}$ bilayers by annealing between 500 and 900 °C for 120 s. (a)–(f) AFM top-views ($5 \times 5\ \mu m^2$). (a-1) − (f-1) Magnified color-coded AFM side-views ($1 \times 1\ \mu m^2$) along with cross-sectional line-profiles. (g)–(i) Plots of Rq and SAR and at %. (j)–(k) EDS spectra at 500 and 900 °C. (j-1) − (k-1) Corresponding summary of at % and wt % of Ag and Pt. (For interpretation of the references to color in this figure legend, the reader is referred to the Web version of this article.)

LSPR intensity as compared to the AgPt of similar size. It was also found that the simulated extinction maxima was blue-shifted to 630 nm, which was in trend with the experimental observation although the peak position was slightly red-shifted from the measured spectra. In addition, the corresponding reflectance spectra are presented in Fig. 3(b), which exhibited two strong absorptions dips at UV and VIS regions for the AgPt NPs due to the HO and MP resonance modes as discussed. However, with the small size Pt NPs the absorption dips were removed clearly in Fig. 3(b), which can be correlated to the enhanced backscattering with the small sized Pt NPs [37]. It can also be correlated to the major contribution from the DR in the case of small and uniform Pt NPs. The average reflectance was decreased at an increased Ta due to the gradual reduction of surface coverage. Furthermore, the transmittance spectra of AgPt and Pt NPs are presented in Fig. 3(c). With the AgPt NPs fabricated between 500 and 500 °C, the UV and VIS region exhibited shoulders. Since the size of AgPt nanoclusters was large, the absorption dips in the transmittance spectra can be

superimsed by the high forward scattering with the quadrupolar resonance being more significant than others. However, with the formation of small and isolated Pt NPs, the absorption dips were gradually developed in the UV and VIS regions due to the QR and DR resonance modes as discussed. Based on the reduced surface coverage by the NPs, the average transmittance was gradually reduced as a function of Ta. As compared with the previous report of Pt on sapphire, the LSPR properties of AgPt and Pt NPs were found to be significantly improved and dynamic, which can be correlated to the improved size, shape and uniformity by introducing the Ag component [31].

Fig. 4 shows the evolution of network-like AgPt NPs to the widely isolated Pt NPs with the $Ag_{42\ nm}/Pt_{9\ nm}$ bilayers by annealing between 600 and 900 °C for 120 s. In this set, since the initial bilayer thickness was increased by three times as compared to the previous set, the dewetting extent was largely altered. With the increased bilayer thickness, generally, the rate of dewetting can be decreased due to the large volume of atoms and thus the resulting

nanostructures generally possess a larger size with the lower density [38]. For instance, only small void and grain structures were obtained at between 500 and 550 °C as observed in Fig. 4(a) − 4(b). The void size was increased up to 500 nm while the void rims started to develop due to the faster agglomeration of atoms around the edges. When the Ta was increased up to 650 °C, the network-like AgPt nanoclusters were formed as seen in Fig. 4(c). A rapid surface morphology transformation was observed at this stage, which can be due to the enhanced agglomeration of alloyed atoms along with the Ag sublimation. The average height of network-like AgPt nanoclusters was increased up to 140 nm while the lateral width was reduced. The Rq and SAR in Fig. 4(g) and (h) also showed a sharp increase between 500 and 600 °C as the network-like AgPt nanoclusters were evolved from layered structures. The at % of Ag and Pt plotted in Fig. 4(i) − 4(k) clearly show the decreasing at % of Ag between 500 and 650 °C due to the sublimation of Ag atoms. Specifically, the at % of Ag was decreased from 92.35 to 75.63% as the network-like AgPt nanoclusters were evolved from the layered structures.

A drastic change in the surface morphology was observed at 750 °C when the large number of isolated small NPs were formed as shown in Fig. 4(d). The breakdown of connected nanoclusters into the isolated ones can be due to the reduction of surface energy and Rayleigh-like instability as discussed [39]. In addition, due to the extensive sublimation of Ag atoms between 650 and 750 °C, the average size of NPs was sharply decreased. At the Ta above 750 °C, the Ag atoms were completely sublimated as indicated by the at % plot in Fig. 4(i). Thus, the NPs fabricated at higher Ta (>750 °C) were of pure Pt, which is also clearly suggested by the EDS spectra in Fig. 4(i) − 4(k). Higher temperature was necessary for the complete Ag atom sublimation due to 3x increased amount as compared with the previous set. It was also found that the irregular configuration of Pt NPs was gradually transformed into the spherical shape and the uniformity was largely improved between 750 and 900 °C as displayed in Fig. 4(e) − 4(f). The average diameter and height of Pt NPs were 130 nm in height and 400 nm in diameter although minor increment in NPs size was observed above 800 °C. Similarly, the Rq and SAR were gradually reduced up to 750 °C and then mildly increased along with the size improvement of NPs. As compared to the previous set, the Pt NPs were found to be widely spaced and larger in size due to the increased bilayer thickness.

Fig. 5 shows the optical properties of AgPt and Pt NPs fabricated with the Ag$_{42 nm}$/Pt$_{9 nm}$ bilayers. Generally, the NPs in this set were larger and widely spaced with the different elemental composition of AgPt and Pt as compared to the previous set, which exhibited the discrete optical behaviors. As seen in the extinction spectra in Fig. 5(a), the AgPt nanostructures between 500 and 650 °C demonstrated the absorption peaks at UV and VIS region due to the
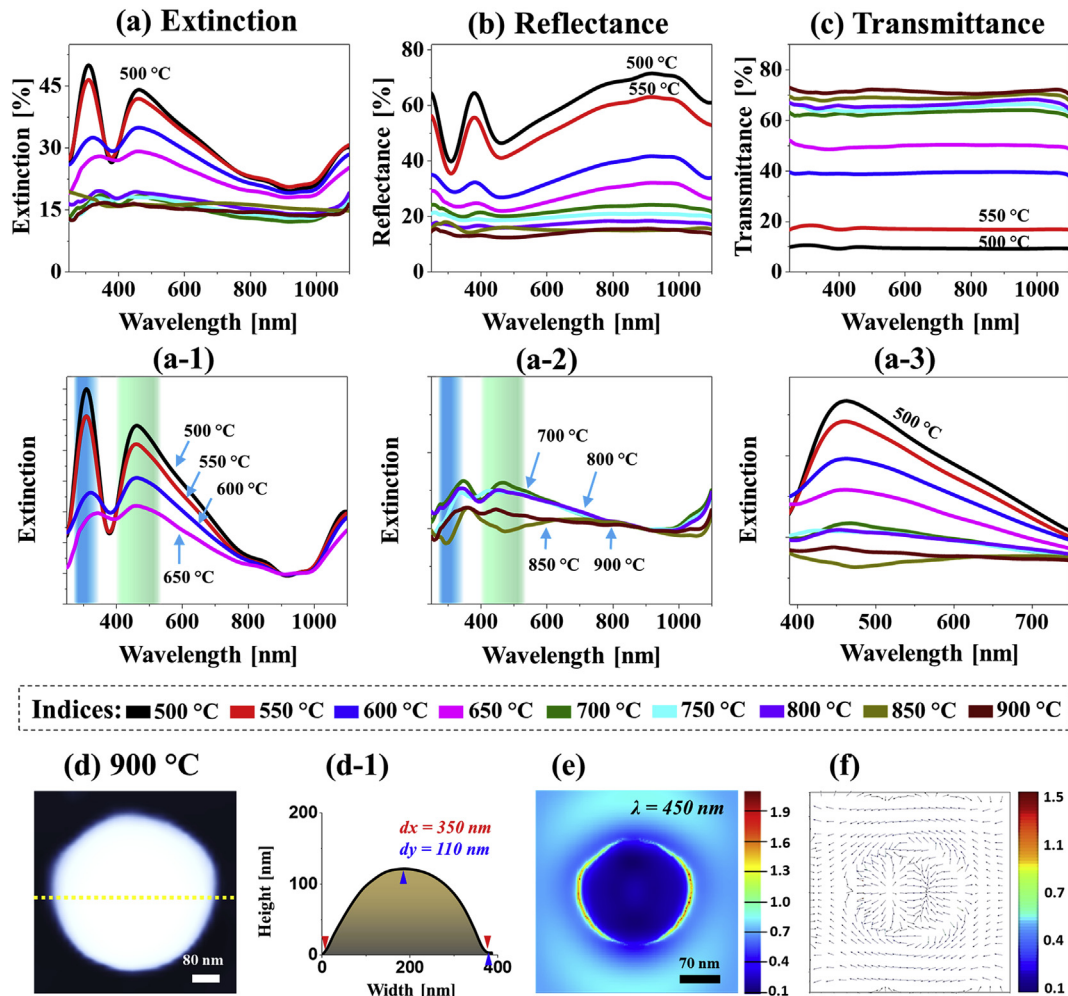

Fig. 5. LSPR properties of AgPt alloy and Pt NPs fabricated with the Ag$_{42 nm}$/Pt$_{9 nm}$ bilayers. (a)−(c) Extinction, reflectance and transmittance spectra. (a-1) − (a-3) Normalized extinction spectra. (d) AFM images of the typical Pt NP at 900 °C. (d-1) Cross-sectional line profile. (e) E-field profile in xy-plane. (f) E-field vector plot.

higher order (HO) and multi-polar (MP) resonance modes respectively [40]. As compared to the previous set, the absorption intensity was found to be much enhanced, which could be due to the larger size of nanostructures and high Ag content. With the gradual evolution of the interconnected AgPt nanoclusters and Ag sublimation, the intensity of LSPR peaks was gradually reduced as clearly evidenced by the attenuated intensity of HO and MP peaks in Figs. 5(a-1). With the formation of pure Pt NPs above 700 °C, the HO (~355 nm) and MP (~445 nm) resonance peaks were further attenuated as shown in Figs. 5(a-2), indicating the less plasmonic response with the pure Pt NPs than the AgPt nanoclusters [37]. Specifically, the MP resonance peak was sharply decreased and flattened with the isolated Pt NPs as displayed by the magnified spectra in Figs. 5(a-3).

The local e-field distribution of typical Pt NP is simulated as shown in Fig. 5(d) − 5(f), which showed a strong e-field confinement at the NP/sapphire interface with the formation of lobes on both sides of NPs. With the typical Pt NP, the e-field was found to be

stronger in the VIS wavelength due to the stronger MP resonance in the VIS region. The simulated extinction power spectra in Fig. S4 also exhibited a shoulder in the UV-VIS region with the maximum at ~450 nm. As shown in Fig. 5(f), the e-field vectors clearly demonstrated the multiple directions along the NP geometry likely due to the excitation of MP resonance modes. The corresponding reflectance spectra of AgPt alloy and Pt NPs is presented in Fig. 5(b). Based on the two different type of NPs, i.e. AgPt and Pt NPs, the reflectance spectra also demonstrated distinctive plasmonic responses. In particular, the AgPt nanostructures exhibited the absorption dips at UV and VIS regions, which corresponds to the HO and MP resonance modes as discussed. The absorption by the AgPt nanostructures was gradually reduced along with the sublimation of Ag atoms as well as reduced surface coverage at the increased Ta. Consequently, with the formation of isolated Pt NPs, very minor absorption dips were observed at HO and MP mode, which can be likely due to the weaker plasmonic responses of Pt NPs as well as the increased backscattering along with the reduced
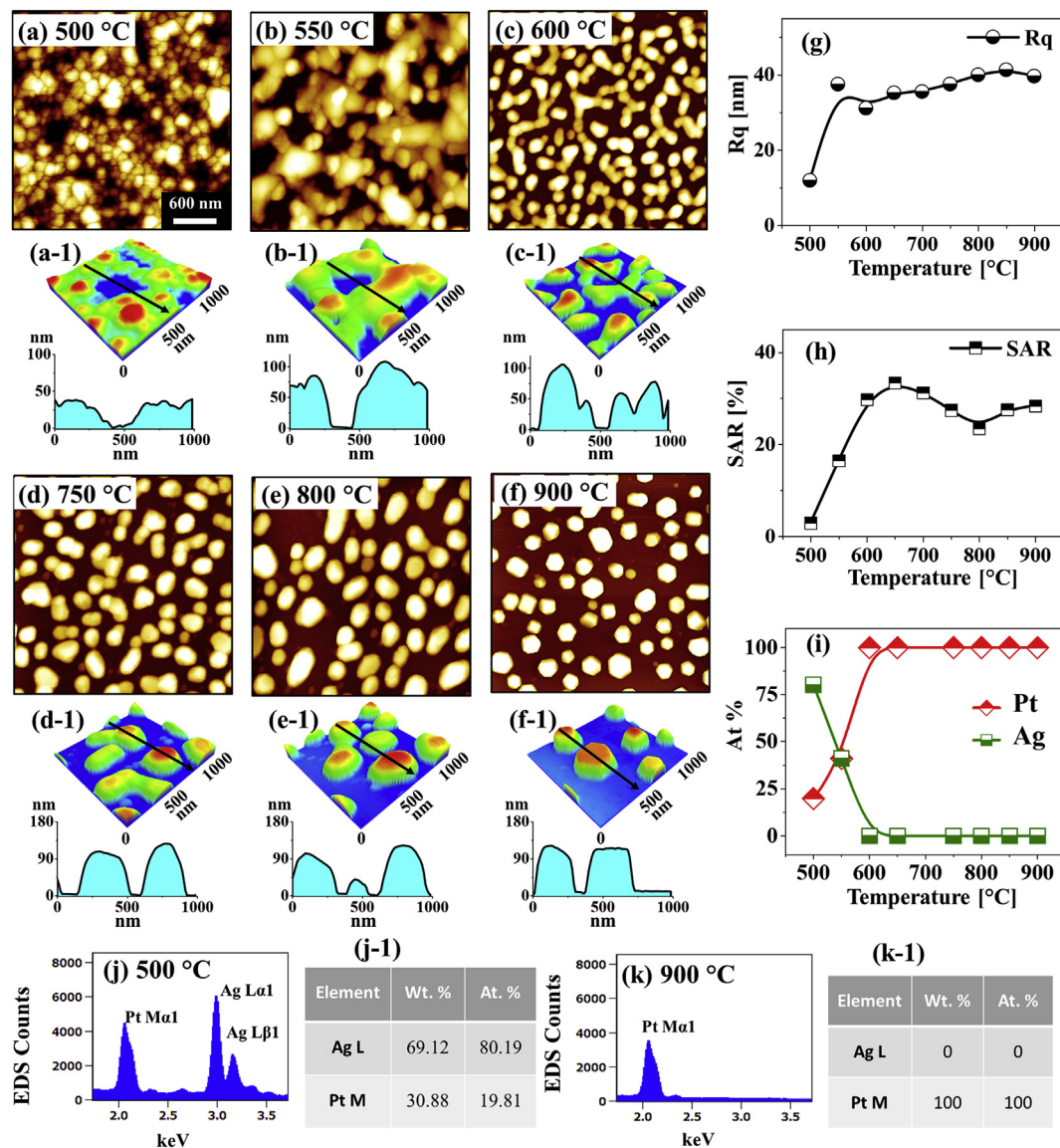

Fig. 6. Evolution of self-assembled AgPt and Pt nanostructures with the $Ag_{50\,nm}/Pt_{25\,nm}$ bilayer annealed between 500 and 900 °C for 120 s. (a)−(f) AFM top-views ($3 \times 3\,\mu m^2$). (a-1) − (f-1) Magnified color-coded AFM side-views ($1 \times 1\,\mu m^2$) along with cross-sectional line-profiles. (g)−(i) Plots of Rq and SAR and at %. (j)−(k) EDS spectra at 500 and 900 °C. (j-1) − (k-1) Summary of at % and wt % of Ag and Pt. (For interpretation of the references to color in this figure legend, the reader is referred to the Web version of this article.)
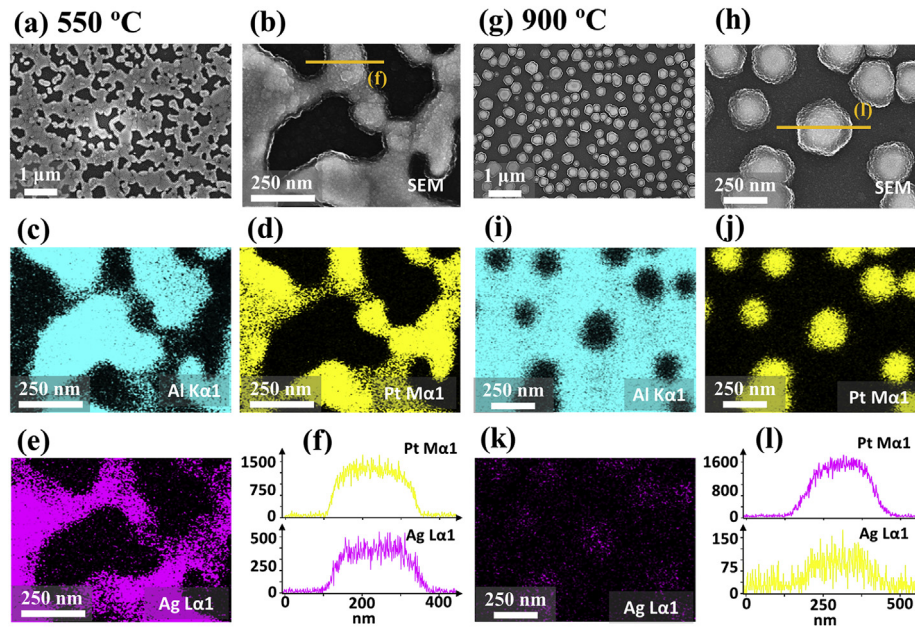
Fig. 7. Elemental mapping of the AgPt and Pt nanoparticles fabricated with the $Ag_{50\ nm}/Pt_{25\ nm}$ bilayer annealed at 500 and 900 °C for 120 s. (a)–(b) SEM images of AgPt nanoclusters. (c)–(e) Elemental phase mapping of Al, Pt and Ag. (f) Line profile through the nanocluster region as indicated in (b). (g)–(h) SEM images of Pt NPs. (i)–(k) Corresponding elemental phase mapping. (l) EDS line profile through Pt NP in (h).

size. In addition, the transmittance spectra in Fig. 5(c) generally demonstrated the flat response in the entire range of wavelength. The wavelength corresponding to the HO and MP resonance mode also did not show the absorption dips, which can be likely due to the pronounced forward scattering of larger NPs. Since the particle size was generally larger than 300 nm in average, the LSPR can be mainly dominated by the quadrupolar resonance and thus high forward scattering can be expected [37].

Fig. 6 presents the evolution of medium size self-assembled AgPt nanoclusters and Pt NPs from the $Ag_{50\ nm}/Pt_{25\ nm}$ bilayer films by the systematic control of Ta. In this set, the ratio of Ag to Pt was decreased to 2 : 1 as compared to the previous 5.4 : 1 and the Pt thickness was increased. Obviously, the dewetting behavior was varied as compared with the previous sets and thus the different configuration and structure of AgPt and Pt NPs were obtained. Along with the enhanced diffusion and alloying of Ag and Pt atoms at increased Ta, the grain-void to the well-developed hexagonal nanocrystal were fabricated in this set. In specific, annealing between 500 and 550 °C resulted in the evolution of voids and granular structures as displayed in Fig. 6(a) and (b). In fact, these voids were significantly smaller in size but greater in number than the previous set. From the cross-sectional line profiles, the average surface height was between 50 and 100 nm as shown in Figs. 6(a-1) and 6(b-1). Due to the variation in the ratio of Ag and Pt atoms, the surface nanostructures were evolved distinctly. For instance, the initial stage of dewetting formed grains and many cracks in this set while only few voids were observed in the previous set. In addition, the Rq and SAR also showed increasing values with the evolution of void and grain between 500 and 550 °C as shown in Fig. 6(g) and (h). To examine the elemental distribution after annealing, the sample annealed 550 °C was further analyzed with high resolution elemental mapping in Fig. 7(a) − 7(f). As seen in Fig. 1(a) − 1(d), the elemental maps of Ag and Pt reveals that the Ag and Pt atoms were intermixed along with the dewetting of nanoclusters. In addition, the EDS line profile through nanocluster in Fig. 7(b) clearly show the homogeneous distribution of Ag and Pt. This clearly indicates that the elements are well intermixed in the nanoclusters, which

can be further improved at higher temperature.

Along with increased Ta, the Ag sublimation was found to be much quicker as shown in Fig. 6(i). For instance, the at % of Ag was decreased from 80.19 to 58.88% when the temperature increased from 500 to 500 °C. At higher Ta, similarly, the at % of Ag was zero indicating complete sublimation. Despite the thicker Ag layer in this set (50 nm as compared to 14 nm), the Ag sublimation occurred much faster likely due to the evolution of large number of voids on the film. When the temperature was increased to 600 °C, the connected Pt NPs were resulted as observed in Fig. 6(c). These NPs had an average height and diameter of ~100 and 500 nm respectively. As the Ta was increased between 750 and 800 °C, the isolated Pt NPs were resulted by the fragmentation of large Pt nanoclusters as shown in Fig. 6(d) and (e). In high temperature regime, the Pt NPs gradually became semi-spherical and more isolated in order to attain the low energy configuration. Finally, the hexagonal shape of Pt NPs was obtained at 900 °C as shown in Fig. 6(f). The elemental phase maps and EDS line profiles in Fig. 7(g) − 7(l) clearly demonstrated that the NPs only contain Pt atoms. From the Ag phase maps, line profiles and at %, it was confirmed that the Ag atoms were completely sublimated, resulting in the well-structured Pt NPs. The average height and diameter of Pt NPs in this temperature range were ~100 nm and 300 nm respectively. The Rq showed minor enhancement up to 850 °C as the NPs were agglomerated more compactly, which resulted in the vertical height increment. In terms of SAR, it was decreased between 650 and 800 °C as the size and density of NPs was reduced but slightly increased above 850 °C with minor size increment. Overall, these Pt NPs were much denser and slightly smaller than those obtained in the previous sets with the much thicker Pt layer. Thus, it can be stated that the Ag thickness as well as overall Ag/Pt bilayer thickness can be varied to realized various size and shape of Pt NPs.

Fig. 8 shows the optical analysis of AgPt and Pt NPs fabricated with the $Ag_{50\ nm}/Pt_{25\ nm}$ bilayer films. In comparison with the previous sets, the nanostructures were denser and larger in size in this set and thus resulted in a distinct LSPR response. Fig. 8(a) shows the extinction spectra of AgPt and Pt NPs, which exhibited
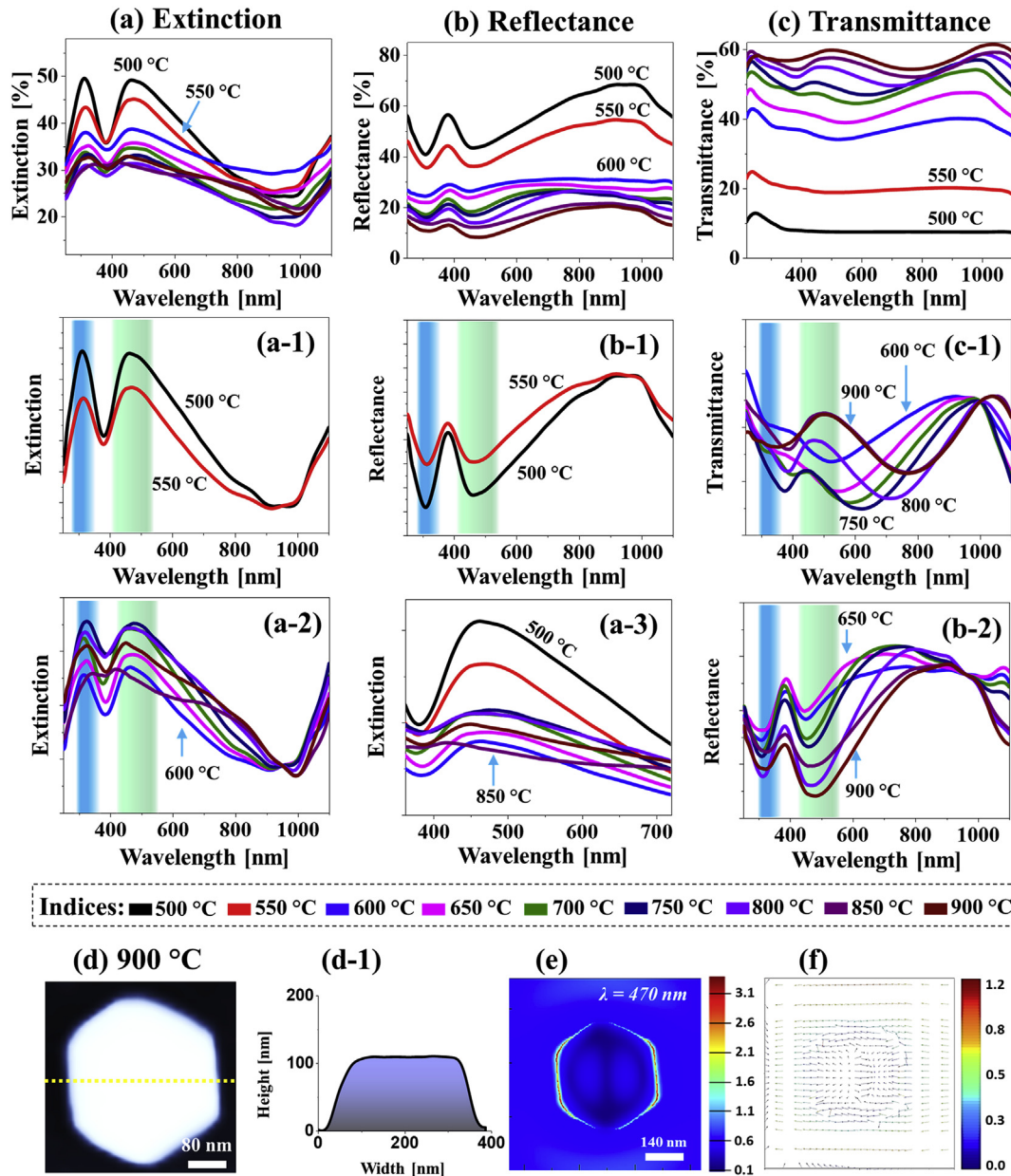
Fig. 8. (a)–(c) Extinction, reflectance and transmittacne spectra of various AgPt alloy and Pt NPs on fabricated with the Ag$_{50\ nm}$/Pt$_{25\ nm}$ films. (a-1) − (a-3) Normalized extinction. (b-1) − (b-2) Normalized reflectance. (c-1) Normalized transmittance. (d) AFM image of the typical Pt NP at 900 °C. (d-1) Cross-sectional line profile. (e) E-field profile in xy-plane. (f) E-field vector plot.

the strong HO resonance peak at ∼ 315 nm and MP resonance peak at ∼ 460 nm. Similar to the previous cases, the resonance peak intensity was reduced along with the decreased average size of NPs and Ag sublimation at increased Ta as depicted in Figs. 8(a-1). Furthermore, the LSPR properties were sharply changed for AgPt nanocluster and Pt NPs as shown in Figs. 8(a-1) and 8(a-2). For instance, although both the HO and MP resonance peaks were observed in all samples, the LSPR intensity with Pt NPs was decreased as compared to AgPt nanostructures. As compared to the pure Pt NPs in the previous sets, the large and much denser Pt NPs in this set exhibited stronger LSPR responses in the UV and VIS regions. Within the temperature range 600 and 900 °C, the LSPR intensity was slightly enhanced as shown in Figs. 8(a-2) as the size and uniformity of NPs was mildly increased. It was also observed that the LSPR peaks were broadened with the pure Pt NPs as

compared to that of AgPt nanoclusters as shown in Figs. 8(a-3), which indicates the weaker LSPR response with Pt NPs [41].

The corresponding reflectance spectra of the larger AgPt and Pt NPs are shown in Fig. 8(b)–8(b-2). Generally, two strong absorption dips were observed with the AgPt and Pt NPs due to the HO and MP resonance in the UV and VIS regions respectively [40]. For the Pt NPs between 600 and 900 °C, the absorption was sharply attenuated as compared to the AgPt NPs at lower Ta. In the case of transmittance spectra in Fig. 8(c) and (c-1), the AgPt nanostructures showed almost flat spectral shape, which can be due to the pronounced forward scattering by the large nanostructures [37]. However, the Pt NPs exhibited the dip and shoulder in the UV and VIS region as shown in Figs. 8(c-1), which can be due to the variation in the contribution of multiple resonance modes. In specific, with the connected and irregular Pt NPs between 600 and 750 °C,

the broad absorption dip was observed and that of isolated and uniform Pt NPs showed two absorption dips. This could be likely due to the splitting of resonance modes on the Pt NPs surface depending upon the shape and uniformity. On the other hand, the shoulder was still persistent in the VIS region as can be expected with large size Pt NPs due to the high forward scattering. The e-field distribution on the typical hexagonal Pt NPs is simulated in Fig. 8(d) − 8(f), which clearly shows the strong field confinement at the sharp boundary. The corresponding extinction power spectrum is included in Fig. S14 in which the extinction shoulder with peak at ~470 nm can be clearly observed. Further, the e-field vector plot in Fig. 8(f) demonstrated the multiple directions along with the symmetry of Pt NPs due to the excitation of MP resonance in the VIS region.

4. Conclusion

In summary, a noble approach of utilizing various Ag/Pt bilayer designs have been successfully demonstrated on sapphire (0001) for the fabrication of AgPt and Pt NPs. The Ag/Pt bilayer configuration significantly accelerated the SSD degree and produced the AgPt nanoclusters at lower annealing temperature and well-defined Pt NPs at higher temperature. The $Ag_{14\ nm}/Pt_{3\ nm}$ and $Ag_{42\ nm}/Pt_{9\ nm}$ bilayers yield the connected AgPt alloy and widely spaced round Pt NPs. The thicker Ag film the $Ag_{50\ nm}/Pt_{25\ nm}$ bilayers markedly enhanced the dewetting and much denser yet larger Pt NPs were formed at the identical annealing temperature regime. The evolution of AgPt bimetallic and pure Pt NPs was discussed based on the inter-mixing, alloying, enhanced diffusion and sublimation of Ag atoms. The AgPt and Pt NPs of various size and configurations exhibited tunable LSPR responses in the UV and VIS wavelength. The AgPt nanoclusters at lower annealing temperature generally showed stronger LSPR responses due to high LSPR activity of Ag and it was gradually reduced along with the Ag sublimation. Meanwhile, the LSPR response of Pt NPs in this study was still stronger in comparison with the previous Pt NPs formed with the pure Pt films due to well defined configuration and larger size.

Acknowledgments

Appendix A. Supplementary data

Supplementary data to this article can be found online at https://doi.org/10.1016/j.jallcom.2019.152193.

References

[1] K.L. Kelly, E. Coronado, L.L. Zhao, G.C. Schatz, The Optical Properties of Metal Nanoparticles: the Influence of Size, Shape, and Dielectric Environment, 2003.

[2] S. Mostafa, F. Behafarid, J.R. Croy, L.K. Ono, L. Li, J.C. Yang, B.R. Cuenya, Shape-dependent catalytic properties of Pt nanoparticles, J. Am. Chem. Soc. 132 (44) (2010) 15714−15719.

[3] L. Lu, Z. Luo, T. Xu, L. Yu, Cooperative plasmonic effect of Ag and Au nanoparticles on enhancing performance of polymer solar cells, Nano Lett. 13 (1) (2012) 59−64.

[4] G. Lozano, S.R. Rodriguez, M.A. Verschuuren, J.G. Rivas, Metallic nanostructures for efficient LED lighting, Light Sci. Appl. 5 (6) (2016) e16080.

[5] S. Dong, J. Shenglin, Y. Muni, Z. Guangzu, L. Huan, L. Minag-Yu, Facile fabrication of the configuration controllable self-assembled Al nanostructures as UV SERS substrates, Nanoscale 10 (2018) 22737−22744.

[6] L. Ji, J. Wang, S. Zuo, Z. Chen, In situ preparation of Pt nanoparticles supported on N-doped carbon as highly efficient electrocatalysts for hydrogen production, J. Phys. Chem. C 121 (16) (2017) 8923−8930.

[7] H.M. So, J. Kim, W.S. Yun, J.W. Park, J.J. Kim, D.J.,. Won, C. Lee, Molecule-based single electron transistor, Phys. E Low-dimens. Syst. Nanostruct. 18 (1−3) (2003) 243−244.

[8] V. Subramanian, E.E. Wolf, P.V. Kamat, Catalysis with TiO2/gold nanocomposites. Effect of metal particle size on the Fermi level equilibration, J. Am. Chem. Soc. 126 (15) (2004) 4943−4950.

[9] Ming-Yu Li, Muni Yu, Su Dong, Jianbing Zhang, Shenglin Jiang, Jiang Wu, Qingping Wang, Sisi Liu, Ultrahigh responsivity UV photodetector based on Cu nanostructure/ZnO QD hybrid architectures, Small (2019) 1901606.

[10] Z. Duan, G. Henkelman, Calculations of CO oxidation over a Au/TiO2 catalyst: a study of active sites, catalyst deactivation, and moisture effects, ACS Catal. 8 (2) (2018) 1376−1383.

[11] E. Hutter, J.H. Fendler, Exploitation of localized surface plasmon resonance, Adv. Mater. 16 (19) (2004) 1685−1706.

[12] M. Yao, X. Jia, Y. Liu, W. Guo, L. Shen, S. Ruan, Surface plasmon resonance enhanced polymer solar cells by thermally evaporating Au into buffer layer, ACS Appl. Mater. Interfaces 7 (33) (2015) 18866−18871.

[13] Ping Shen, Yan Liu, Yongbing Long, Liang Shen, Bonan Kang, High-performance polymer solar cells enabled by copper nanoparticles-induced plasmon resonance enhancement, J. Phys. Chem. C 120 (16) (2016) 8900−8906.

[14] Peng Xu, Liang Shen, Fanxu Meng, Jiaqi Zhang, Wenfa Xie, Wenjuan Yu, Wenbin Guo, Xu Jia, Shengping Ruan, The role of Ag nanoparticles in inverted polymer solar cells: surface plasmon resonance and backscattering centers, Appl. Phys. Lett. 102 (2013), 53,12.

[15] Mengnan Yao, Ping Shen, Yan Liu, Boyuan Chen, Wenbin Guo, Shengping Ruan, Liang Shen, Performance improvement of polymer solar cells by surface-energy-induced dual plasmon resonance, ACS Appl. Mater. Interfaces 8 (9) (2016) 6183−6189.

[16] Ping Shen, Guoxin Wang, Bonan Kang, Wenbin Guo, Liang Shen, High-efficiency and high-color-rendering-index semitransparent polymer solar cells induced by photonic crystals and surface plasmon resonance, ACS Appl. Mater. Interfaces 10 (7) (2018) 6513−6520.

[17] N.T. Nguyen, S. Ozkan, O. Tomanec, X. Zhou, R. Zboril, P. Schmuki, Nanoporous AuPt and AuPtAg alloy co-catalysts formed by dewetting−dealloying on an ordered TiO2 nanotube surface lead to significantly enhanced photocatalytic H2 generation, J. Mater. Chem. A 6 (28) (2018) 13599−13606.

[18] A. Naldoni, M. D'Arienzo, M. Altomare, M. Marelli, R. Scotti, F.,. Morazzoni, V. Dal Santo, Pt and Au/TiO2 photocatalysts for methanol reforming: role of metal nanoparticles in tuning charge trapping properties and photoefficiency, Appl. Catal. B Environ. 130 (2013) 239−248.

[19] P. Pandey, M. Sui, Q. Zhang, M.Y. Li, S. Kunwar, J. Lee, Systematic control of the size, density and configuration of Pt nanostructures on sapphire (0 0 0 1) by the variation of deposition amount and dwelling time, Appl. Surf. Sci. 368 (2016) 198−207.

[20] J.M. Lee, B.I. Kim, Thermal dewetting of Pt thin film: etch-masks for the fabrication of semiconductor nanostructures, Mater. Sci. Eng. A 449 (2007) 769−773.

[21] D. Rakić, A.B. Djurišic, J.M. Elazar, M.L. Majewski, Optical properties of metallic films for vertical-cavity optoelectronic devices, Appl. Opt. 37 (1998) 5271−5283.

[22] E.D. Palik (Ed.), Handbook of Optical Constants of Solids, vol. 3, Academic press, 1998.

[23] Guang Yang, Xiao-Jian Fu, Jing-Bo Sun, Ji Zhou, Spectroscopic ellipsometry study on the optical dielectric properties of silver platinum alloy thin films, J. Alloy. Comp. 551 (2013) 352−359.

[24] Minhee Kang, Myeong-Su Ahn, Youngseop Lee, Ki-Hun Jeong, Bioplasmonic alloyed nanoislands using dewetting of bilayer thin films, ACS Appl. Mater. Interfaces 9 (42) (2017) 37154−37159.

[25] A. Herz, F. Theska, D. Rossberg, T. Kups, D. Wang, P. Schaaf, Solid-state dewetting of Au−Ni bi-layer films mediated through individual layer thickness and stacking sequence, Appl. Surf. Sci. 444 (2018) 505−510.

[26] A. Herz, A. Franz, F. Theska, M. Hentschel, T. Kups, D. Wang, P. Schaaf, Solid-state dewetting of single-and bilayer Au-W thin films: unraveling the role of individual layer thickness, stacking sequence and oxidation on morphology evolution, AIP Adv. 6 (3) (2016), 035109.

[27] P.R. Gadkari, A.P. Warren, R.M. Todi, R.V. Petrova, K.R. Coffey, Comparison of the agglomeration behavior of thin metallic films on Si O 2, J. Vac. Sci. Technol. A: Vac. Surf. Films 23 (4) (2005) 1152−1161.

[28] G. Seguini, J.L. Curi, S. Spiga, G. Tallarida, C. Wiemer, M. Perego, Solid-state dewetting of ultra-thin Au films on SiO2 and HfO2, Nanotechnology 25 (49) (2014) 495603.

[29] J. Quan, J. Zhang, X. Qi, J. Li, N. Wang, Y. Zhu, A study on the correlation between the dewetting temperature of Ag film and SERS intensity, Sci. Rep. 7 (1) (2017) 14771.

[30] A. Herz, D. Wang, T. Kups, P. Schaaf, Solid-state dewetting of Au/Ni bilayers: the effect of alloying on morphology evolution, J. Appl. Phys. 116 (4) (2014), 044307.

[31] Mao Sui, Ming-Yu Li, Sundar Kunwar, Puran Pandey, Quanzhen Zhang, Jihoon Lee, Effects of annealing temperature and duration on the morphological and optical evolution of self-assembled Pt nanostructures on c-plane sapphire, PLoS One 12 (5) (2017) e0177048.

[32] Puran Pandey, Sundar Kunwar, Mao Sui, Ming-Yu Li, Quanzhen Zhang, Jihoon Lee, Effect of annealing temperature on morphological and optical

transition of silver nanoparticles on c-plane sapphire, J. Nanosci. Nanotechnol. 18 (5) (2018) 3466—3477.

[33] D. Lahiri, B. Bunker, B. Mishra, Z. Zhang, D. Meisel, C.M.,. Doudna, T. Shibata, Bimetallic Pt—Ag and Pd—Ag nanoparticles, J. Appl. Phys. 97 (9) (2005), 094304.

[34] Yong Ding, Fengru Fan, Zhongqun Tian, Zhong Lin Wang, Sublimation-induced shape evolution of silver cubes, Small 5 (24) (2009) 2812—2815.

[35] P. Pandey, S. Kunwar, M. Sui, S. Bastola, J. Lee, Compositional effect on the fabrication of AgxPd1— x alloy nanoparticles on c-plane sapphire at distinctive stages of the solid-state-dewetting of bimetallic thin films, RSC Adv. 7 (87) (2017) 55471—55481.

[36] Christoph Langhammer, Zhe Yuan, Igor Zorić, Bengt Kasemo, Plasmonic properties of supported Pt and Pd nanostructures, Nano Lett. 6 (4) (2006) 833—838.

[37] C. Langhammer, B. Kasemo, I. Zorić, Absorption and scattering of light by Pt, Pd, Ag, and Au nanodisks: absolute cross sections and branching ratios, J. Chem. Phys. 126 (19) (2007) 194702.

[38] S. Kunwar, P. Pandey, M. Sui, S. Bastola, J. Lee, Morphological and optical properties of PdxAg1-x alloy nanoparticles, Sci. Technol. Adv. Mater. 19 (1) (2018) 160—173.

[39] F. Ruffino, E. Carria, S. Kimiagar, I. Crupi, M.G. Grimaldi, Rayleigh-instability-driven dewetting of thin Au and Ag films on indium—tin-oxide surface under nanosecond laser irradiations, Micro & Nano Lett. 8 (3) (2013) 127—130.

[40] K. Lance Kelly, Eduardo Coronado, Lin Lin Zhao, George C. Schatz, The Optical Properties of Metal Nanoparticles: the Influence of Size, Shape, and Dielectric Environment, 2003, pp. 668—677.

[41] S. Kunwar, M. Sui, Q. Zhang, P. Pandey, M.Y. Li, J. Lee, Various silver nano-structures on sapphire using plasmon self-assembly and dewetting of thin films, Nano-Micro Lett. 9 (2) (2017) 17.